

1     **Estimation of Shortwave Direct Radiative Forcing of Biomass Burning**  
2                     **Aerosols using New Angular Models**

3

4

5

6                     Xiang Li, Sundar A. Christopher, Joyce Chou, and Ronald M. Welch

7

8                             Department of Atmospheric Sciences

9                             University of Alabama in Huntsville

10                                 Huntsville, AL 35806

11

12

13

14

15

16

Revised Version

17                     Submitted to Journal of Applied Meteorology: Special Issue on TRMM

18                                     March, 2000

19

20

21

22

23

24

25

26

---

27     **Corresponding Author:**

28     Xiang Li

29     Department of Atmospheric Sciences

30     University of Alabama in Huntsville

31     Huntsville, AL 35806

32     [xli@atmos.uah.edu](mailto:xli@atmos.uah.edu)

33     Phone: (256) 922-5969

34     Fax: (256) 922-5723

35

1  
2  
3  
4  
5  
6  
7  
8  
9  
10  
11  
12  
13  
14  
15  
16  
17

### **Abstract**

Using a new angular distribution model (ADM) for smoke aerosols, the instantaneous Top-of-Atmosphere (TOA) Shortwave Aerosol Radiative Forcing (SWARF) is calculated for selected days over biomass burning regions in South America. The Visible and Infrared Scanner (VIRS) data is used to detect smoke aerosols and the Cloud and Earth Radiant Energy System (CERES) scanner data from the Tropical Rainfall Measuring Mission (TRMM) is used to obtain the broadband radiances. First, the ADM for smoke aerosols is calculated over land surfaces using a discrete-ordinate radiative transfer model. The instantaneous TOA shortwave (SW) fluxes are estimated using the new smoke ADM and compared with the SW fluxes from the CERES product. The RMS error between the CERES SW fluxes and fluxes using the smoke ADM is  $13 \text{ Wm}^{-2}$ . The TOA SWARFs per unit optical thickness for the 6 surface types range from  $-29 \text{ Wm}^{-2}$  to  $-57 \text{ Wm}^{-2}$ , showing that smoke aerosols have a distinct cooling effect. The new smoke ADM developed as part of this study could be used to estimate radiative impact of biomass burning aerosols.

## 1 **1. Introduction**

2 Biomass burning is considered to be one of the major sources of trace gas species  
3 and tropospheric aerosol particles (Crutzen et al., 1979). These aerosols play a significant  
4 role in atmospheric chemistry (Andreae, 1991), earth radiation budget (Penner et al.,  
5 1992; Hobbs et al., 1997) and climate (IPCC, 1995). Widely prevalent in the tropics,  
6 anthropogenic biomass burning has expanded drastically in the last 15 years due to  
7 increased deforestation practices in Brazil's Amazon basin, as well as to clear land for  
8 shifting cultivation in South America, Southeast Asia and Africa (Seiler and Crutzen,  
9 1980). It is estimated that 114 Tg of smoke is released into atmosphere yearly through  
10 biomass burning, out of which 80% is in the tropical regions (Penner et al., 1992; Hao  
11 and Liu, 1994).

12 Smoke aerosols from biomass burning can significantly modify the earth's  
13 radiation budget (Penner et al. 1992; Hobbs et al. 1997; Christopher et al. 1996). Smoke  
14 aerosols, mainly composed of organic matters and black carbon (Martins et al. 1998),  
15 reflect and absorb the solar radiation and therefore have a direct radiative effect. They  
16 also serve as cloud condensation nuclei (CCN) and have an indirect radiative effect by  
17 modulating the cloud properties. The direct smoke shortwave (SW) Aerosol Radiative  
18 Forcing (SWARF) at the top-of-atmosphere (TOA), defined as the difference of TOA  
19 SW fluxes between clear-sky and smoke conditions, is a measure of direct aerosol SW  
20 radiative impact due to biomass burning events. If TOA SW flux over a smoke aerosol  
21 region is larger than that over clear-sky condition, the TOA SWARF is negative. As a  
22 result, if SWARF is negative it implies that more solar radiation is reflected back to space  
23 at smoke condition and therefore is called a "cooling effect". Important parameters

1 include the rate of biomass burning, the lifetime of smoke, the fraction of burned material  
2 that goes into smoke, the surface albedo, the fractional cloud cover, the fraction of smoke  
3 that is distributed between land and ocean, and the optical properties of aerosols that  
4 include single scattering albedo, optical depth, and extinction coefficients. Using these  
5 parameters, the direct TOA SWARF of smoke aerosols can be estimated using a simple  
6 radiative transfer equation (Penner et al., 1992; Hobbs et al., 1997). However, due to the  
7 uncertainty in smoke aerosol characteristics, the estimate of direct TOA SWARF for  
8 smoke aerosols is uncertain. The estimated global-mean values of TOA SWARF due to  
9 biomass burning aerosols are  $-0.8 \text{ Wm}^{-2}$  (Penner et al., 1992) and  $-0.3 \text{ Wm}^{-2}$  (Hobbs et al.,  
10 1997), respectively. The TOA SWARF difference between the Penner et al.(1992) and  
11 Hobbs et al.(1997) estimates is the result of assuming different values of the scattering  
12 and absorption efficiencies and the humidification factor of biomass burning aerosols.

13         Satellite measurements provide a more straightforward approach of estimating  
14 regional and global TOA SWARF values for smoke aerosols. Using the combination of  
15 Advanced Very High Resolution Radiometer (AVHRR) and the Earth Radiation Budget  
16 Experiment (ERBE) (Barkstrom, 1984) measurements, the instantaneous direct TOA  
17 SWARFs for smoke aerosols were estimated over South America by Christopher et al.  
18 (1996, 1998). More recently, this approach has been extended using Tropical Rainfall  
19 Measuring Mission (TRMM) data sets (Christopher et al., 2000). Depending upon aerosol  
20 concentrations, the instantaneous SWARF can be as high as  $-70 \text{ Wm}^{-2}$ .

21         Measurements from the ERBE instruments on board NOAA polar-orbiting  
22 satellites and the Earth Radiation Budget Satellite (ERBS) provided important data sets  
23 for the understanding of the Earth Radiation Budget. This effort of measuring TOA

1 radiative fluxes continues through the subsequent Cloud and Earth's Radiant Energy  
2 System (CERES) instruments on board of TRMM platform and the upcoming Earth  
3 Observing System (EOS) satellites. In both the ERBE and the CERES scanner products,  
4 broadband shortwave (SW) (0.2 – 5.0  $\mu\text{m}$ ) and longwave (LW) (5.0 – 50  $\mu\text{m}$ ) radiances  
5 were measured by the scanners. The measured radiances were converted to SW and LW  
6 fluxes using the Angular Distribution Models (ADM), which relates the TOA radiances  
7 at a specific solar and observing geometry to the TOA fluxes under various surface and  
8 atmospheric conditions. There are a total of 12 ERBE ADMs, derived by combining 5  
9 surface types (ocean, land, snow, desert, mixed, or coastal) with 4 cloud conditions  
10 (clear, partly cloudy, mostly cloudy, and overcast) (Green, 1987). Although the TOA  
11 radiances were accurately measured with careful calibration procedures, the accuracy of  
12 ERBE TOA fluxes were affected by the accuracy of ERBE ADMs, as well as the scene  
13 identification, which determines the proper ERBE ADM to be used. Suttles et al. (1992)  
14 showed that the estimated SW albedo systematically increases with increasing viewing  
15 zenith angle, and LW fluxes decreases with increasing viewing zenith angle due to  
16 limitations in the ERBE ADM. The limited number of ERBE ADMs also limits the  
17 accuracy of converted ERBE fluxes. To overcome these problems, the CERES team is  
18 developing a new generation of CERES ADMs (Green et al. 1995). It is expected that  
19 increased accuracy of CERES cloud property determination and the new ADMs can  
20 reduce the uncertainty in the flux conversion by a factor of 3 to 4 (Wielicki et al., 1995).  
21 However, note that in both the ERBE and the CERES projects, the angular distribution  
22 model for smoke is not available. Lacking proper scene categories, smoke aerosols are  
23 usually classified as either clear or partly cloudy in the ERBE and CERES products. Due

1 to strong absorption of smoke aerosols on solar radiation and differences in particle size  
2 distributions between clouds and smoke, the ADMs for clouds and smoke could be  
3 significantly different. This may cause uncertainties in the estimation of TOA SW fluxes  
4 over biomass burning regions in the ERBE and the CERES products. Therefore, an ADM  
5 for smoke aerosols will improve the accuracy of CERES SW fluxes over biomass  
6 burning regions.

7         In this paper, we calculate an ADM for smoke aerosols and examine the ADM  
8 impact on the TOA SW fluxes over biomass burning regions in the CERES product.  
9 First, a plane-parallel discrete-ordinate radiative transfer model is used to calculate the  
10 smoke ADM using optical properties of smoke aerosols obtained from the Smoke, Cloud  
11 and Radiation-Brazil (SCAR-B) experiment (Kaufman et al. 1998). The calculated smoke  
12 ADM is a function of aerosol optical properties, surface albedo and solar and satellite  
13 viewing geometry. Using VIRS imagery, smoke pixels are detected, and the optical  
14 thickness of the detected smoke pixels is retrieved. The TOA SW fluxes for smoke  
15 aerosols are obtained using the measured CERES radiances and the calculated ADMs for  
16 smoke aerosols. Then, we compare the calculated TOA SW fluxes for smoke aerosols  
17 with those obtained from the CERES ES8 ERBE-like data product. Finally, we estimate  
18 the instantaneous TOA SWARF over smoke regions based on the local ecosystems and  
19 compare the differences of the TOA SWARFs computed using the calculated TOA SW  
20 fluxes and using the CERES ES8 ERBE-like data product. This is one of the first  
21 attempts to estimate the uncertainty of instantaneous smoke TOA SWARF caused by the  
22 uncertainty in angular distribution models.

1           In section 2, the VIRS and the CERES data products used in this study are  
2 introduced. Section 3 presents the calculation of smoke ADMs using the radiative  
3 transfer model and then compares the calculated ADM for smoke aerosols with some of  
4 the ERBE ADMs. The sensitivity of the calculated ADMs to aerosol optical properties  
5 and surface albedos are examined. Results and analyses are shown in section 4. The  
6 instantaneous TOA SWARFs of smoke aerosols are estimated, and comparisons are made  
7 for smoke TOA SWARFs between using the calculated ADM and the CERES data  
8 product. Section 5 concludes the paper.

9

## 10 **2. Satellite data and study area**

11           The TRMM provides detailed and comprehensive data sets for the studies of the  
12 distribution of rainfall and latent heating, as well as atmosphere's radiation budget in  
13 tropics. Two TRMM data sets are used in this study: 1) VIRS Level 1B, and 2) CERES  
14 ES8 ERBE-like product. We focus on the 1998 burning season over land in South  
15 America in August 1998. The area of study is between 35°S – 5°N and 80°W – 40°W.

16

### 17 **2.1 VIRS Level 1B data**

18           The Visible and Infrared Scanner (VIRS) measures reflected solar and emitted  
19 terrestrial radiation in five spectral channels. The central wavelengths of the five channels  
20 are 0.63, 1.61, 3.75, 10.8, and 12.0  $\mu\text{m}$ , respectively, with spatial resolution of 2.11 km at  
21 nadir (Kummerow et al. 1998). In this study, the version 4 of VIRS Level 1B data  
22 product is used. The Level 1B data set contains calibrated radiances measured from the  
23 five channels of the instrument. The channel 1 and 2 radiances are converted to

1 reflectances, and the channel 3, 4 and 5 radiances are converted to brightness  
2 temperatures. Since the measured radiances in the 3.75  $\mu\text{m}$  channel contain contributions  
3 from both solar and thermal components, a sixth channel (channel 3 reflectance) is  
4 created by removing the thermal emission part using the 10.8 channel  $\mu\text{m}$  channel  
5 information (Kaufman and Nakajima, 1993). The VIRS radiometer is calibrated using  
6 ground testing and in-flight data. In-flight calibration of channels 1 and 2 is accomplished  
7 via an onboard solar diffuser and by using the moon as a calibration source (Keiffer and  
8 Wildey, 1996) and calibration of channels 3, 4 and 5 is accomplished via an onboard  
9 blackbody and a space view (Kummerow et al. 1998).

10

## 11 **2.2 CERES ES8 ERBE-like data**

12 The CERES scanner on the TRMM platform is a broadband instrument (Wielicki  
13 et al., 1996) that measures the total (0.3 – 50  $\mu\text{m}$ ), SW (0.3 – 5.0  $\mu\text{m}$ ) and LW (5.0 – 50.0  
14  $\mu\text{m}$ ) radiances. The measured radiances are converted to fluxes using ADM's (Suttles et  
15 al. 1988; 1989) developed as part of the ERBE project and is called CERES ES-8 ERBE-  
16 like product. In this study, the Level 2 CERES ES-8 ERBE-like data set is used. The  
17 CERES scanner has two scanning modes: the normal cross-track scanning mode, and the  
18 rotational scanning mode. In this study, only CERES ES8 ERBE-like data from the cross-  
19 track scanning mode are used.

20

## 21 **2.3 Collocation of VIRS and CERES**

22 The VIRS data product includes measurements at five narrow spectral channels  
23 with a spatial resolution of about 2 km at nadir. It can be used to identify smoke pixels

1 and to retrieve optical properties of smoke aerosols (Christopher et al. 2000). On the  
 2 other hand, the CERES data product provides TOA radiative fluxes at a reduced spatial  
 3 resolution. Collocating the two data products is necessary to establish the relation  
 4 between aerosol optical properties and the TOA SWARF for smoke aerosols. For a VIRS  
 5 pixel and a CERES footprint to be considered collocated, the geographical difference  
 6 between the VIRS pixel and the center of the CERES footprint must be less than  $0.02^\circ$ .  
 7 Both the spatial resolution of a CERES footprint and the spatial resolution of a VIRS  
 8 pixel change with scanning angle. For example, at nadir, the spatial resolution of a  
 9 CERES footprint is 8 km in the across-track and 16 km in the along-track direction; at a  
 10 scan angle of  $63^\circ$  towards the edge of the swath, the spatial resolutions increase to 116  
 11 km and 16 km in the across and along direction, respectively (Green and Wielicki, 1995).  
 12 The collocation procedure accounts for the change of the CERES and VIRS pixel sizes  
 13 with scanning angle.

14

### 15 **3. Angular Distribution Model (ADM) for smoke aerosols**

16 The measured radiance from the CERES scanner at specific sun-satellite angle is  
 17 converted to TOA flux (Green et al., 1995) using the following equation:

$$F_{TOA}^{\uparrow} = \frac{\pi I(\theta_0, \theta, \phi)}{\xi(\theta_0, \theta, \phi)} \dots \dots \dots (1),$$

18 where  $I(\theta_0, \theta, \phi)$  is the sensor-measured radiance at solar zenith angle  $\theta_0$ , satellite zenith  
 19 angle  $\theta$ , and relative azimuth angle between Sun and satellite  $\phi$ ,  $\xi(\theta_0, \theta, \phi)$  is the angular  
 20 distribution model(ADM) value that relates radiance to flux at specific solar and satellite  
 21 viewing geometry, and  $F_{TOA}^{\uparrow}$  is the TOA upward flux at  $0.3 - 5.0 \mu\text{m}$  for SW channel.  
 22 As a result, the accuracy of converted TOA SW fluxes over biomass burning regions  
 23 depends upon the accuracy of the ADMs for smoke aerosols.

1           A discrete-ordinate radiative transfer model called SBDART (Ricchiuzzi et al.,  
2 1997), is used to calculate the shortwave (0.28 – 4.0  $\mu\text{m}$ ) ADMs for horizontally  
3 homogeneous smoke aerosols over different surface types. The SBDART is a detailed  
4 plane-parallel radiative transfer code based on the discrete ordinate approach (Stamnes et  
5 al. 1988). The radiative processes included in the model are Rayleigh scattering, gaseous  
6 absorptions, cloud and aerosol scattering and absorptions. Gaseous absorptions are  
7 considered in the model based on the low-resolution band models developed for the  
8 LOWTRAN 7 atmospheric transmission code (Pierluissi and Marogoudakis, 1986). In  
9 order to use gas transmission functions in DISORT, the band models are approximated  
10 with a three-term exponential fit (Wiscombe and Evans, 1977). The SBDART model can  
11 compute the radiative effects of several common boundary layer and upper-level  
12 atmosphere aerosol types, including rural, urban, or maritime aerosols in the boundary  
13 layer, as well as fresh and aged volcanic aerosols in the upper atmosphere. User-defined  
14 aerosol types are allowed in the SBDART model, which is characterized by the spectral  
15 aerosol extinction coefficient ( $\sigma_e$ ), aerosol single scattering albedo ( $\omega_0$ ), and asymmetry  
16 factor ( $g$ ).

17           The spectral optical properties of smoke aerosols used in this study are obtained  
18 from the SCAR-B experiment. The smoke particles are modeled as organic liquid shell  
19 with black carbon cores (Ross et al. 1998). The volume size distribution of smoke  
20 aerosols is assumed to be lognormal with a mode radius of 0.15  $\mu\text{m}$  (Remer et al. 1998).  
21 Smoke particles are assumed to be spheres, which is well supported by SCAR-B  
22 measurements (Martins et al. 1998), and Mie theory applied to stratified spheres  
23 (Ackerman and Toon 1981) is used to calculate the light scattering and absorption

1 coefficients of the smoke aerosols. Figure 1 shows the single scattering albedo and  
2 asymmetry factor as the function of wavelength. The curves at 3.0-4.0  $\mu\text{m}$  are  
3 extrapolated from the curves at 0.30-3.0  $\mu\text{m}$  since Ross et al (1998) provide values only  
4 up to 3.0  $\mu\text{m}$ .

5 In the smoke ADM calculations, a standard tropical atmosphere (McClatchey et  
6 al. 1972) is assumed. The surface is assumed to be Lambertian and the uncertainty of this  
7 assumption is discussed later in this section. In this study, we refer to the calculated  
8 ADM for smoke aerosols as *smoke ADM*. The smoke ADM is a function of  $\tau$ ,  $\omega_0$ ,  
9 broadband surface albedo ( $\alpha_s$ ),  $\theta_0$ ,  $\theta$ , and  $\phi$ . The  $\tau$  and  $\omega_0$  values are specified at 0.64  $\mu\text{m}$   
10 unless stated otherwise. The aerosol values of  $\tau$  are calculated in the range from 0.36 to  
11 3.6 in steps of 0.36. The four  $\omega_0$  values are 0.70, 0.79, 0.82, and 0.85, respectively that is  
12 well within the range of measurements (Reid et al. 1998). There are 10 solar zenith  
13 angles with cosine of the angles decreasing from 0.90 to 0.45 in steps of 0.05. There are  
14 15 satellite zenith angles with cosines of the angles decreasing from 1.0 to 0.3 in steps of  
15 0.05. Values of  $\phi$  range from  $0^\circ$  to  $180^\circ$  intervals of  $22.5^\circ$ . There are four values of  $\alpha_s$ :  
16 0.10, 0.15, 0.20, and 0.25, covering the range for the surface types in biomass burning  
17 regions.

18 Figures 2a–d show the calculated ADMs for aerosol values of  $\tau$  of 0.36, 1.1, 1.8,  
19 and 2.5, respectively. The aerosol  $\omega_0$  value is assumed to be 0.85 that is the average value  
20 of regionally aged aerosols (Reid et al. 1998),  $\alpha_s$  is assumed to be 0.15, and solar zenith  
21 angle is assumed to be  $36.9^\circ$ . The relative azimuth angle of  $0^\circ$  represents the forward  
22 direction of scattering. From Figures 2a–d, the ADM value increases with increasing  
23 satellite zenith angle. When the  $\tau$  value is 0.36, the ADM values in the forward scattering

1 direction ( $\varphi=0^\circ$ ) increase from 0.87 to 1.34 and values in the backward scattering  
2 direction ( $\varphi=180^\circ$ ) increase from 0.87 to 1.11 as  $\theta$  values increase from  $0^\circ$  to  $69.5^\circ$ .  
3 When the  $\tau$  value increases from 0.36 to 2.5, the ADM values in the forward direction  
4 increase from 0.83 to 1.49 and values in the backward direction increase from 0.83 to  
5 0.96 as  $\theta$  values increase from  $0^\circ$  to  $69.5^\circ$ . The range of ADM values in the forward  
6 direction increases and values in the backward direction decreases with increasing value  
7 of  $\tau$ . Comparison of Figures 2c and 2d shows no significant difference between the two  
8 ADMs, indicating that the smoke ADM is not sensitive to the value of  $\tau$  when  $\tau$  is larger  
9 than 1.8 (heavy smoke concentration). Figures 2e and 2f show smoke ADMs with same  
10  $\omega_0$  and solar zenith angle as in Figure 2a and 2c, but with the value of  $\alpha_s$  increased from  
11 0.15 to 0.20. The  $\tau$  values for Figures 2e and 2f are 0.36 and 1.8, respectively.  
12 Comparison of Figures 2f and 2c, with  $\tau = 1.8$ , shows no large difference between the  
13 two ADMs, indicating that when aerosol  $\tau$  is large, the smoke ADM is less dependent on  
14 the surface albedo (surface type). Comparison of Figures 2e and 2a, with  $\tau = 0.36$ , shows  
15 large differences in the smoke ADMs. In the forward and backward scattering directions,  
16 the ADM values in Figure 2e range from 0.91 to 1.28 and from 0.91 to 1.07, respectively.  
17 Comparing to Figure 2a, the range of ADM values decreases in both the forward and  
18 backward scattering directions because for small aerosol  $\tau$  value, the surface albedo has a  
19 greater impact on the smoke ADM. Figures 2g and 2h shows the smoke ADMs with same  
20  $\tau$ ,  $\omega_0$  and  $\alpha_s$  values as in Figures 2e and 2f, correspondingly, but with solar zenith angle  
21 increased from  $36.9^\circ$  to  $60^\circ$ . In Figure 2h, the ADM values range from 0.73 to 2.12 and  
22 from 0.73 to 0.90, respectively, in the forward and backward scattering directions as  $\theta$

1 values increase from  $0^\circ$  to  $69.5^\circ$ . Comparison of Figures 2f and 2h shows that the ranges  
2 of smoke ADM values in the forward scattering direction significantly increases with  
3 increasing solar zenith angle. With larger solar zenith angle, the smoke ADM is less  
4 isotropic.

5 Since most of smoke-occupied CERES footprints are classified as either clear or  
6 partly cloudy in the ES8 ERBE-like data product, we compare the smoke ADMs with  
7 two ERBE ADMs: clear over land as shown in Figure 2i, and partly cloudy over land as  
8 shown in Figure 2j, for solar zenith angle of  $60^\circ$ . Although the ranges of ADM values are  
9 similar between smoke ADMs and ERBE ADMs, the patterns of the two types of ADMs  
10 are different. The ERBE ADMs are more sensitive to azimuth-angle. The ERBE clear  
11 ADM (Figure 2i) has larger ranges of values in the forward and backward scattering  
12 angles than that for smoke ADM at  $\tau$  value of 0.36. Comparison of Figures 2h and 2j  
13 shows that the range of smoke ADM values is larger than that of the ERBE ADM in the  
14 forward scattering direction, and is smaller than that of the ERBE ADM in the backward  
15 scattering direction. The mean absolute difference between the ADMs in Figures 2g and  
16 2i is 0.102, and the relative difference is 10.3%. The mean absolute difference between  
17 the ADMs in Figures 2h and 2j is 0.101, the relative difference is 9.8%.

18 Using new ADM's for cloudy conditions, Lubin and Webber (1995) showed that  
19 the net surface SW fluxes under cloud condition over the ocean surfaces are different  
20 from the ERBE ADMs by  $20\text{-}60 \text{ Wm}^{-2}$ . The surface radiative fluxes are often estimated  
21 from the TOA radiative fluxes using some established relationships from atmospheric  
22 radiative transfer (Li et al. 1993). In biomass burning regions, a 10% uncertainty in TOA  
23 SW fluxes can cause significant errors of surface SW fluxes since smoke aerosols are

1 normally less reflective than clouds and most of the incoming solar fluxes reach the  
 2 surface. Therefore, smoke ADMs are necessary to improve the accuracy of estimated SW  
 3 fluxes, especially at the surface.

4         Since the smoke ADM is a function of  $\tau$ ,  $\omega_0$ ,  $\alpha_s$ , uncertainties in these values  
 5 cause uncertainties of the smoke ADM values. Since the TOA clear-sky albedo is  
 6 directly related to  $\alpha_s$  in clear-sky conditions, the sensitivity of smoke ADM to the  
 7 parameters of  $\tau$ ,  $\omega_0$ , and TOA clear-sky albedo is examined. Figure 3a shows the ADM  
 8 value as the function of smoke  $\tau$  value. The  $\omega_0$ , TOA clear-sky albedo and  $\theta$  values are  
 9 0.85, 0.15 and  $40^\circ$ , respectively. The solar zenith angles are assumed to be  $30^\circ$  and  $60^\circ$ ,  
 10 respectively. The relative azimuth angles are assumed to be  $45^\circ$  (forward scattering) and  
 11  $135^\circ$  (backward scattering), respectively. From Figure 3a, it is seen that the ADM values  
 12 are not sensitive to the values of  $\tau$  when  $\tau$  is larger than 1.7. When  $\tau$  is less than 1.7, the  
 13 ADM values become more sensitive to the  $\tau$  values, especially at the larger solar zenith  
 14 angles. When  $\phi_0$  is  $60^\circ$ , the ADM values vary from 0.97 to 1.04 as the  $\tau$  values vary from  
 15 0.35 to 1.5, an increase of about 7%. Figure 3b shows the ADM values as a function of  
 16  $\omega_0$ . In this case, the  $\tau$  value is 1.1, and TOA clear-sky albedo and solar and satellite  
 17 viewing geometry are the same as the ones in Figure 3a. The ADM values are less  
 18 sensitive to values of  $\omega_0$  when the  $\omega_0$  value is less than 0.81, becoming more sensitive to  
 19  $\omega_0$  as the  $\omega_0$  values become larger than 0.81. The ADM values vary by less than 3%  
 20 when the  $\omega_0$  value varies from 0.76 to 0.85. Figure 3c shows the ADM values as a  
 21 function of TOA clear-sky albedo. The  $\omega_0$  value is 0.85 and  $\tau$  value is 1.1. The solar  
 22 zenith angle, satellite angle and relative azimuth angle are set to be same as in Figures 3a

1 and 3b. From Figure 3c, it is seen that the ADM values are slightly more sensitive to  
2 TOA clear-sky albedo in the backward scattering direction than in the forward scattering  
3 direction. The ADM value varies from 0.92 to 0.97 as clear-sky albedo changes from  
4 0.10 to 0.24, a change of about 5%. In general, we conclude that the smoke ADMs are  
5 relatively insensitive to the smoke optical properties and TOA clear-sky albedos. For  
6 most cases, the uncertainty of smoke ADM is expected to be less than 10% due to the  
7 uncertainties of these parameters.

8         The asymmetry factor, mainly determined by the particle size distribution of  
9 smoke aerosols, has an impact on the reflected solar radiation at the TOA. As a result, the  
10 smoke ADM is affected by the asymmetry factor. Ross et al. (1998) shows that during  
11 SCAR-B g (0.64  $\mu\text{m}$ ) can range from 0.40 to 0.55 for a variety of smoke aerosol size  
12 distributions. The uncertainty of smoke ADM caused by the uncertainty of asymmetry  
13 factor is examined (Figure 4(a)). The  $\omega_0$  and  $\alpha_s$  values are 0.85, 0.15, respectively. The  
14  $\theta_0$ ,  $\theta$  and  $\phi$  values are  $60^\circ$ ,  $40^\circ$  and  $45^\circ$ , respectively. The sensitivity of ADM values to  
15 the asymmetry factor is examined for three  $\tau$  values: 0.35, 1.06 and 1.78. From Figure  
16 4(a), the uncertainty of smoke ADM values caused by the variation of g values are within  
17 2%. The uncertainty of smoke ADM caused by the assumed constant spectral surface  
18 albedo also is examined and shown in Figure 4(b). The  $\omega_0$  value is 0.85. The  $\theta_0$ ,  $\theta$  values  
19 are  $60^\circ$  and  $40^\circ$ , respectively. The  $\phi$  values are  $45^\circ$  and  $135^\circ$ , respectively. In Figure 4(b),  
20 constant albedo means the ADM values are calculated assuming constant spectral surface  
21 albedo with the value of 0.169, while vegetation means the ADM values are calculated  
22 using the vegetation spectral surface albedo as specified in SBDART with the equivalent  
23 broadband albedo of 0.169. From Figure 4(b), the uncertainty of smoke ADM values

1 caused by the uncertainty of spectral surface albedo decreases with increasing  $\tau$  for both  
2 forward scattering direction and backward scattering direction. The uncertainty can be as  
3 high as 5% when  $\tau$  is less than 0.8.

4 The accuracy of smoke ADM is affected by the assumption of Lambertian  
5 surface. From the aircraft measurements during SCAR-B, surface reflectance is found to  
6 be anisotropic over Cerrado and Forest (Tsay et al. 1998). Also, the bidirectional  
7 reflectance distribution functions (BRDF) for Cerrado and Forest surfaces are different.  
8 The uncertainty of smoke ADM caused by the assumption of Lambertian surface is  
9 examined in this study and results are shown in Figure 4(c). Again, the  $\omega_0$  value is  
10 assumed to be 0.85. The  $\theta_0$ ,  $\theta$  values are  $60^\circ$  and  $40^\circ$ , respectively. The  $\phi$  values are  $45^\circ$   
11 and  $135^\circ$ , respectively. Cerrado BRDF means that the smoke ADM values are calculated  
12 using the BRDF over Cerrado as shown in Plate 2 of Tsay et al. (1998). When  $\tau$  is larger  
13 than 0.8, the uncertainty of smoke ADM values is less than 4%. This is expected since  
14 the smoke scattering effect dominates over surface reflectance when  $\tau$  gets large.  
15 However, when  $\tau$  is smaller than 0.5, the uncertainty is significant and can reach about  
16 10%, suggesting that BRDF is necessary to obtain accurate smoke ADM values with light  
17 smoke loading.

18

#### 19 **4. Results and Discussion**

20 The VIRS Level 1B data and the CERES ES8 ERBE-like data in August 1998 are  
21 used to analyze instantaneous smoke TOA SWARF over South America. Table 1 lists the  
22 information of the 14 VIRS data files used in this study, including the observing date,  
23 time and geographical coverage. Smoke can be clearly seen from the channel 1 images of

1 these VIRS data files. Figure 5a shows an example of the channel 1 image of the VIRS  
2 data. In Figure 5a, the lower part of the image clearly shows high cloud amounts.

3 A smoke detection algorithm based on simple thresholds is developed in this  
4 study. This algorithm identifies smoke pixels from the VIRS images over land surfaces  
5 using channel 1 reflectance ( $R_1$ ), channel 2 reflectance ( $R_2$ ), channel 3 reflectance ( $R_3$ ),  
6 channel 4 brightness temperature ( $T_4$ ) and channel 5 brightness temperature ( $T_5$ ). A  
7 number of thresholds are used to identify a VIRS pixel as a cloud, smoke or clear-sky  
8 pixel (Figure 6). First, isolated cumulus clouds are identified using a 5 x 5 window region  
9 around a VIRS pixel. If the standard deviation of channel 1 reflectance ( $\sigma_{R_1}$ ) for the  
10 pixels in the window is larger than 0.04, the window region is labeled as cloud and no  
11 further processing will be done on these pixels. A number of thresholds are sequentially  
12 used to identify bright and thick clouds, high and cold cirrus clouds, low clouds, optically  
13 thick smoke ( $R_1$  is usually over 0.30), dense smoke ( $R_1$  is usually over 0.20), optically  
14 thin smoke haze ( $R_1$  is usually less than 0.20) and clear-sky conditions. The ratio of  $R_2$   
15 to  $R_1$  is used to separate smoke pixels from clear-sky pixels over land. For the vegetation  
16 surface types, surface spectral albedo at 1.6  $\mu\text{m}$  (channel 2) is much higher than that that  
17 at 0.64  $\mu\text{m}$  (channel 1). As a result, the values of  $R_2/R_1$  are usually larger than 2.0. The  
18 existence of smoke aerosols increases channel 1 reflectance and the values of  $R_2/R_1$   
19 decrease. The threshold of 1.9 for  $R_2/R_1$  is used which separates most of the clear-sky  
20 pixels from smoke pixels for the 14 images that were studied. This smoke detection  
21 algorithm works well to identify cloud, smoke and clear-sky pixels for all the 14 VIRS  
22 data files in this study. The accuracy of the detection scheme was tested by visually  
23 comparing the results with the visible imagery from VIRS. Figure 5b shows the scene

1 identification image corresponding to the VIRS image in Figure 5a. The black color  
2 represents clear-sky over lands. The gray color represents clouds, and the white color  
3 represents smoke aerosols. Comparing to Figure 5a, smoke haze, clouds and clear sky  
4 pixels are properly identified.

5 For the smoke pixels detected from the VIRS images, aerosol optical thicknesses  
6 are retrieved using the VIRS channel 1 images. A table look-up approach, the same as the  
7 one used in the retrieval of  $\tau$  from the AVHRR channel 1 images (Li et al., 1999), is used  
8 for the  $\tau$  retrieval. The SBDART model is used to produce the look-up table. Smoke  
9 aerosols are assumed to be spherical with an organic liquid shell and black carbon core.  
10 The particle size distribution of smoke aerosols is assumed to be log-normal. Mie theory  
11 is used to calculate the spectral optical properties of smoke aerosols, and they match well  
12 with the ones obtained from the SCAR-B experiment (Ross et al. 1998). This approach  
13 was validated in the satellite retrieval of  $\omega_0$  during SCAR-B in 1995 burning season. The  
14 retrieved  $\omega_0$  values are in good agreement with the ones obtained from *in-situ* aircraft  
15 measurements during SCAR-B. A detailed description of this retrieval approach is given  
16 in Li et al. (1999).

17 The  $\tau$  values for smoke aerosols are retrieved from the VIRS channel 1 images  
18 assuming the aerosol  $\omega_0$  values based on the surface types defined in the International  
19 Geosphere-Biosphere Programme (IGBP). There are total of 18 surface types, covering  
20 different vegetation surfaces over land, ocean, and ice (Belward and Loveland, 1996).  
21 The radiative impact of smoke over the surface types of forest, savanna, grassland,  
22 wetland, mixed forest and cropland is examined in this study. The  $\omega_0$  values at the  
23 wavelength of  $0.55 \mu\text{m}$  for surface types of forest, savanna, grassland, and wetland are

1 assumed to be 0.881, 0.862, 0.924, 0.892, respectively, which are the mean  $\omega_0$  values for  
2 the corresponding surface types retrieved from the AVHRR imagery during SCAR-B and  
3 the results agree well with the *in-situ* measurements (Reid et al. 1998). For the other  
4 surface types, the  $\omega_0$  value of 0.88 at 0.55  $\mu\text{m}$  is assumed, that is in the  $\omega_0$  range of 0.8 –  
5 0.9 as obtained during SCAR-B (Reid et al. 1998).

6 Surface albedo is a key parameter in both the look-up table for smoke  $\tau$  retrieval  
7 and in the smoke ADMs. Since satellite sensors detect SW radiation at the TOA, the  
8 clear-sky albedo at the TOA can be directly estimated from the satellite observations. In  
9 this study, the SBDART model is used to calculate the relation between TOA albedo and  
10 surface albedo under clear-sky conditions assuming the standard tropical atmosphere  
11 (McClatchey et al. 1972). The result is that the surface albedo can be inferred from the  
12 TOA clear-sky albedo.

13 The VIRS channel 1 TOA clear-sky albedo map is determined as following. The  
14 study area is first divided into 4x4 km grids. The clear sky albedo is determined by  
15 assigning the minimum R1 value obtained from all pixels falling into this grid. All VIRS  
16 data files in August 1998 are used to obtain this clear-sky albedo map.

17 The broadband TOA clear-sky albedo map is determined in three steps. First, the  
18 study area is also divided 20x20 km. If the percentage of clear-sky pixels for a collocated  
19 VIRS-CERES sample is greater than 90%, we assume that this collocated sample is a  
20 clear-sky sample. The broadband TOA clear-sky albedo for a grid is determined to be the  
21 minimum value of broadband TOA albedos for all clear-sky samples in August which fall  
22 into this grid. The broadband TOA albedo for a sample is determined as the ratio of  
23 CERES ES8 ERBE-like SW flux to the downward broadband SW flux at this solar zenith

1 angle. Second, if there are no clear-sky samples available for a grid, the minimum value  
2 out of the four neighboring grid points is used. Third, if the clear-sky albedos are not  
3 available from the four neighboring grids, the TOA clear-sky albedo for the grid is  
4 assigned as a value based on the IGBP surface type. The mean clear-sky albedo for each  
5 of the IGBP surface types are calculated from all clear-sky samples detected in August,  
6 1998. The broadband TOA clear-sky albedos for the 6 surface types of forest, savanna,  
7 grassland, and wetland, mixed forest and cropland are shown in Table 2.

8 For each of the collocated samples, the smoke, cloud and clear-sky percentages  
9 are calculated. A sample is labeled as a smoke sample if the smoke percentage is over  
10 90% within the CERES footprint, and the smoke  $\tau$  value is retrieved using the mean  
11 value of VIRS channel 1 reflectance for this footprint. A total of 23783 collocated data  
12 samples are labeled as smoke samples from the 14 VIRS images investigated, and 20156  
13 of the samples are retrieved with  $\tau$  values between 0.1 to 3.5, which is the range of our  
14 look-up table. For the total of 23783 smoke samples, over 58% of the samples are  
15 identified as clear over land in the CERES ES8 ERBE-like data product and over 39%  
16 are identified as partly cloudy over land. Therefore, almost all smoke samples are  
17 identified as clear and partly cloudy, and the corresponding ERBE ADMs are used to  
18 convert the measured radiance into TOA fluxes in the CERES ES8 ERBE-like product.

19 For each smoke sample, the TOA SW flux is estimated using the smoke ADM.  
20 Figure 7 shows the scatter plot of the SW fluxes converted using the smoke ADM versus  
21 the ES8 ERBE-like SW fluxes. The correlation is over 96%. The mean difference  
22 between the model-estimated fluxes and the ERBE-like fluxes is  $0.48 \text{ Wm}^{-2}$  with  
23 standard deviation of  $12.7 \text{ Wm}^{-2}$ . The RMS error is  $12.7 \text{ Wm}^{-2}$ . The relative mean

1 difference is 15%. Therefore, based on the 14 VIRS data files, there is almost no bias  
 2 between the model-estimated TOA SW fluxes and the ERBE-like SW fluxes. This result  
 3 suggests that on the average, the ERBE ADMs work well in the conversion from  
 4 measured radiances to TOA SW fluxes.

5 For all the smoke samples, values of instantaneous smoke SWARF are calculated  
 6 and grouped, based upon the IGBP surface types. The SWARF of smoke aerosols is  
 7 defined as following:

$$SWARF = F_{SW,clear}^{\uparrow} - F_{SW,smoke}^{\uparrow} \dots \dots \dots (2)$$

8

9 where  $F_{SW,clear}^{\uparrow}$  and  $F_{SW,smoke}^{\uparrow}$  are the TOA upward SW fluxes for clear-sky conditions  
 10 and smoke conditions, respectively.

11 Table 2 shows the instantaneous smoke TOA SWARFs for the major surface  
 12 types over the area of study. The TOA SWARF values estimated from the SW fluxes  
 13 converted from the ERBE ADMs and smoke ADMs for each surface type are given. The  
 14 mean and standard values of retrieved  $\tau$ , and the TOA SWARF per unit optical thickness  
 15 is also given in Table 2. For the forest surface type, the mean value of the TOA SWARF  
 16 using the smoke ADMs is about  $5 \text{ Wm}^{-2}$  larger than that using the ERBE ADMs. The  
 17 relative difference is about 9%. For the grassland surface type, the mean value of the  
 18 TOA SWARF using the smoke ADMs is about  $2 \text{ Wm}^{-2}$  smaller than that using the ERBE  
 19 ADMs. The relative difference is about 6%. For the cropland surface type, the mean  
 20 value of the TOA SWARF using the smoke ADMs is about  $9 \text{ Wm}^{-2}$  smaller than that  
 21 using the ERBE ADMs. The relative difference is over 20%. The TOA SWARFs over  
 22 the six surface types range from  $-32 \text{ Wm}^{-2}$  to  $-55 \text{ Wm}^{-2}$ , indicating that smoke aerosols

1 have a cooling effect. These results are in good agreement with the ones from previous  
2 studies (Christopher et al., 1996, 1998). The ratios of TOA SWARFs per  $\tau$  range from –  
3  $28 \text{ Wm}^{-2}$  to  $-71 \text{ Wm}^{-2}$ . In general, the differences of smoke TOA SWARF values  
4 estimated between using the smoke ADM and using the ERBE ADMs are within  $10$   
5  $\text{Wm}^{-2}$ . The relative differences are within 10%.

6

## 7 **5. Conclusions**

8 Based on measurements made during the SCAR-B experiment, a new ADM is  
9 developed for smoke aerosols from a radiative transfer model. The ADM, a key element  
10 in the CERES program, is used to convert the observed TOA radiances to broadband  
11 fluxes. The calculated smoke ADMs are a function of aerosol  $\tau$ , and  $\omega_0$  values, surface  
12 albedo, solar zenith angle, satellite zenith angle, and the relative azimuth angle between  
13 sun and satellite. Comparisons of smoke ADMs with the ERBE ADMs show that  
14 although the range of the ADM values is similar between the two types of ADM models,  
15 the fine structures are different. The ERBE ADMs are more azimuth-angle sensitive  
16 compared to the smoke ADMs. The relative difference of the ADM value between the  
17 two types of models is about 10% on average. The smoke ADM is not sensitive to the  
18 aerosol  $\tau$  and  $\omega_0$  values or to the surface albedo. The uncertainty of the smoke ADM  
19 value due to uncertainties in these parameters is generally within 10%.

20 Using the collocated Level 1B VIRS data product and the CERES ES8 ERBE-like  
21 data product in August 1998, TOA SW radiative forcing of biomass burning aerosols are  
22 estimated. A threshold technique is first developed to identify smoke, cloud and clear-sky  
23 pixels over land using VIRS channels 1, 2, 3R, 4 and 5. The threshold technique works

1 well and identifies most of the smoke haze from the 14 VIRS images used in this study.  
2 The optical thicknesses of smoke aerosols are retrieved from VIRS channel 1 imagery  
3 using a table look-up approach. Based on the retrieved aerosol optical thickness, the  
4 ADM values for the collocated samples are determined from the pre-calculated look-up  
5 table which is the function of aerosol optical thickness, single scattering albedo, surface  
6 albedo, solar zenith angle, satellite zenith angle and relative zenith angle. The TOA SW  
7 fluxes are then obtained by converting from the observed SW radiances using the smoke  
8 ADM values for the collocated samples.

9 Comparisons are made between the CERES ES8 ERBE-like TOA SW fluxes and  
10 the TOA SW fluxes converted from the observed TOA radiances using smoke ADM. The  
11 correlation between the two data sets is about 96%. The mean difference between the  
12 CERES TOA fluxes and model-estimated fluxes is  $0.48 \text{ Wm}^{-2}$ . The RMS error between  
13 the two data set is  $12.7 \text{ Wm}^{-2}$ .

14 The TOA SWARF values for smoke aerosols are estimated based on the surface  
15 types. The TOA SWARFs range from  $-32 \text{ Wm}^{-2}$  to  $-55 \text{ Wm}^{-2}$ , indicating that smoke  
16 aerosols have a cooling effect. The ratios of TOA SWARFs per unit optical thickness  
17 range from  $-29 \text{ Wm}^{-2}$  to  $-57 \text{ Wm}^{-2}$ . The difference of estimated TOA SWARFs using  
18 CERES SW fluxes and SW fluxes from smoke ADMs are within  $10 \text{ Wm}^{-2}$ . The relative  
19 differences are generally less than 10%.

20

## 21 **Acknowledgements**

22 This research is partially supported by NASA grant NAGW-5195, NAG5-8404  
23 and NASA grant NCC8141 as part of the Global Aerosol Climatology Project. Xiang Li

1 is supported under NASA's Earth System Science Fellowship program (NASA reference  
2 number ESS/98-0000-0115). The CERES data were obtained from the NASA Earth  
3 Observing System Data and Information System, Distributed Active Archive Center  
4 (DAAC) at the Langley Research Center and the VIRS data were obtained through  
5 NASA Goddard Space Flight Center DAAC. We also thank to Drs. Ricchiazzi and  
6 Gautier for making the SBDART code available. Appreciation is extended to Drs. Tsay  
7 and Arnold for providing the BRDF data for cerrado and forest surfaces.

8

## 9 **References**

- 10 Ackerman, T.P., and O. B. Toon, 1981: Absorption of visible radiation in atmosphere  
11 containing mixtures of absorbing and nonabsorbing particles, *Applied Optics*, **20**, pp.  
12 3661-3667
- 13 Andreae, M.O., 1991: Biomass burning: its history, use, and distribution and its impact  
14 on environmental quality and global climate, *Global Biomass Burning*, edited J.S.  
15 Levine, The MIT press
- 16 Barkstrom, B.R., 1984: The Earth Radiation Budget Experiment. *Bull. Amer. Meteorol.*  
17 *Soc.* Vol.65, pp 1170-1185
- 18 Belward, A. and T. Loveland, 1996: The DIS 1km land cover dataset, *Global Change, the*  
19 *IGBP news letter*, **27**
- 20 Christopher, S.A., D.V. Vulcan, J. Chou, and R.M. Welch, 1996: First estimates of the  
21 radiative forcing of aerosols from biomass burning from satellite data, *J. Geophys. Res.*,  
22 101, 21256-21273

- 1 Christopher, S.A., M. Wang, T.A. Berendes, R.M. Welch, and S.K. Yang, 1998: The  
2 1985 biomass burning season in South America: Satellite remote sensing of fires,  
3 smoke, and regional radiative energy budget, *J. Applied Meteor.* 37(7), 661-678.
- 4 Christopher, S.A., J. Chou, J. Zhang, X. Li and R.M. Welch, 2000: Shortwave Direct  
5 Radiative Forcing of Biomass Burning Aerosols Estimated From VIRS and CERES.  
6 Submitted to Geophysical Research Letters.
- 7 Crutzen, P.J., L.E. Heidt, J.P. Kransiec, W.H. Pollack, and W. Seiler, 1979: Biomass  
8 burning as a source of atmospheric gases CO, H<sub>2</sub>, N<sub>2</sub>, CH<sub>3</sub>Cl, and COS, *Nature*, 282,  
9 253-256
- 10 Green, R.N., 1987: Earth Radiation Budget Experiment (ERBE) Data Management  
11 System Processed Archival Tape S-8 PAT users's guide, NASA Langley Research  
12 Center
- 13 Green, R.N., B.A. Wielicki, J.A. Coakley III, L.L. Stowe, and P.O'R. Hinton, 1995:  
14 Clouds and the Earth's Radiant Energy System(CERES) Algorithm Theoretical Basis  
15 Document, Subsystem 4.5, *NASA reference Publication* 1376, Vol.III
- 16 Green, R.N., and B.A. Wielicki, 1995: Clouds and the Earth's Radiant Energy  
17 System(CERES) Algorithm Theoretical Basis Document, Subsystem 4.4, *NASA*  
18 *reference Publication* 1376, Vol.III
- 19 Hao, W.M., and M.-H. Liu, 1994: Spatial and temporal distribution of biomass burning,  
20 *Global Biogeochemical Cycles*, 8, pp 495-503
- 21 Hobbs, P.V., J.S. Reid, R.A. Kotchenruther, R.J. Ferek, R. Weiss, 1997: Direct radiative  
22 forcing by smoke from biomass burning, *Science*, 275, 1776-1778
- 23 IPCC, 1995: Climate Change 1995, *Cambridge University Press*

- 1 Kaufman, Y. J., and T. Nakajima, 1993: Effect of Amazon smoke on cloud microphysics  
2 and albedo – Analysis from satellite imagery, *J. Appl. Meteorol.*, **32**, pp. 729-744
- 3 Kaufman, Y.J., P.V. Hobbs, V.W.J.H. Kirchhoff, P. Artaxo, L.A. Remer, B.N. Holben,  
4 M.D. King, E.M. Prins, D.E. Ward, K.M. Longo, L.F. Mattos, C.A. Nobre, J.D.  
5 Spinhirne, Q. Ji, A.M. Thompson, J.F. Gleason, S.A. Christopher, and S.-C. Tsay, 1998:  
6 The Smoke, Cloud and Radiation Experiment in Brazil (SCAR-B), *J. Geophys. Res.*,  
7 Vol.103, D24, 31783-31808
- 8 Keiffer, H. H, and R. L. Wildey, 1996: Establishing the moon as aspectral radiance  
9 standard. *J. Atmos. Oceanic Technol.*, **13**, 360-375
- 10 Kummerow, C., W. Barnes, T. Kozu, J. Shuie, and J. Simpson, 1998: TheTropical  
11 Rainfall Measring Mission (TRMM) Sensor package. *J. Atmos.Oceanic Tech.*, **15**, 809-  
12 817
- 13 Li, X., S.A. Christopher, J. Zhang, J. Chou, and R. M. Welch, 1999: Aerosol single  
14 scattering albedo estimated from NOAA-14 AVHRR measurements: Case studies over  
15 Brazil, *Proceedings of SPIE*, Denver, CO July 18-23
- 16 Lubin, D., and P.G. Weber, 1995: The use of cloud reflectance functions with satellite  
17 data for surface radiation budget estimation, *J. Appl. Meteorol.*, 34, pp 1333-1347
- 18 Martins, J.V., P. Artaxo, C. Liousse, J. S. Reid, P. V. Hobbs, and Y. J. Kaufman, 1998:  
19 Effects of black carbon content, particle size, and mixing on light absorption by aerosols  
20 from biomass burning in Brazil, *J. Geophys. Res.* **103**, pp. 32,041-32,050
- 21 McClatchey, R.A., R.W. Fenn, J.E.A. Selby, F.E. Volz, J.S. Garing, 1972: Optical  
22 properties of the atmosphere, Air Force Cambridge Research Laboratories Report  
23 AFCRL-72-0497.

- 1 Penner, J.E., R.E. Dickinson, and C.A. O'Neill, 1992: Effects of aerosols from biomass  
2 burning on the global radiation budget, *Science*, 256, 1432-1433
- 3 Pierluissi, J.H., and C.E. Maragoudakis, 1986: Molecular transmission band models for  
4 LOWTRAN, AFGL-TR-86-0272, AD A180655.
- 5 Reid, J. S., P. V. Hobbs, R. J. Ferek, D. R. Blake, J. V. Martins, M. R. Dunlap, and C.  
6 Liousse, 1998: Physical, chemical, and optical properties of regional hazes dominated by  
7 smoke in Brazil, *J. Geophys. Res.* **103**, 32,059-32,080
- 8 Remer, L.A., Y. J. Kaufman, B. N. Holben, A. M. Thompson, and D. McNamara, 1998:  
9 Biomass burning aerosol size distribution and modeled optical properties, *J. Geophys.*  
10 *Res.*, **103**, pp. 31,879-31,891, 1998
- 11 Ricchiuzzi, P. J., S. Yang, C. Gautier, and D. Sowle, 1998: SBDART: a practical tool for  
12 plane-parallel radiative transfer in the Earth's atmosphere, *Bull. Amer. Meteorol. Soc.* **79**,  
13 pp. 2101-2114
- 14 Ross, J. L., P. V. Hobbs, and B. Holben, 1998: Radiative characteristics of regional hazes  
15 dominated by smoke from biomass burning in Brazil: Closure tests and direct radiative  
16 forcing, *J. Geophys. Res.*, **103**, pp. 31,925-31,941
- 17 Sailer, W., and P.J. Crutzen, 1980: Estimates of gross and net fluxes of carbon between  
18 the biosphere and atmosphere from biomass burning, *Climate Change*, 2, 207-247
- 19 Stamnes, K., S. Tsay, W. Wiscombe, and K. Jayaweera, 1988: Numerically stable  
20 algorithm for discrete-ordinate-method radiative transfer in multiple scattering and  
21 emitting layered media, *Appl. Opt.*, 27, 2502-2509

- 1 Suttles, J.T., R.N. Green, P. Minnis, G.L. Smith, W.F. Staylor, B.A. Wielicki, I.J. Walker,  
2 D.F. Young, V.R. Taylor, and L.L. Stowe, 1988: Angular Radiation Models for Earth-  
3 Atmosphere System. I-Shortwave Radiation. NASA RP-1184
- 4 Suttles, J.T., R.N. Green, G.L. Smith, B.A. Wielicki, I.J. Walker, V.R. Taylor, and L.L.  
5 Stowe, 1989: Angular Radiation Models for Earth-Atmosphere System. II-longwave  
6 Radiation. NASA RP-1184
- 7 Suttles, J.T., B.A. Wielicki, and V. Sastri, 1992: Top-of-Atmosphere radiative fluxes –  
8 validation of ERBE scanner inversion algorithm using Nimbus-7 ERB data, *J. Appl.*  
9 *Meteorol.* Vol. 31, No 7, 784-796
- 10 Tsay, S-C. M.D. King, G.T. Arnold, and J.Y. Li, 1998: Airborne spectral measurements  
11 of surface anisotropy during SCAR-B, *J. Geophys. Res.*, **103**, pp. 31,943-31,953
- 12 Wielicki, B.A., R.N. Green, C.J. Tolson, and A. Fan, 1995: *Clouds and the Earth's*  
13 *Radiant Energy System(CERES) Algorithm Theoretical Basis Document, Subsystem 4.0*
- 14 Wielicki, B. A., B. R. Barkstrom, E. F. Harrison, R.B. Lee III, G. L. Smith and J. E.  
15 Cooper, 1996: Clouds and the Earth's Radiant Energy System (CERES): An Earth  
16 Observing System Experiment, *Bull. Amer. Meteor. Soc.*, 77, 853-868
- 17 Wiscombe, W.J., J.W. Evans, 1977: Exponential-sum fitting of radiative transmission  
18 functions, *J. Comp. Physics*, 24, 416-24,444
- 19  
20  
21  
22  
23

1

2 Table 1. A list of VIRS data files used in the smoke detection and smoke SWARF forcing investigation

3

4

5

6

7

8

9

10

11

12

13

14

15

16

17

18

19

20

21

22

23

24

25

26

27

Table 2. The mean broadband TOA clear-sky albedo, the statistics for the retrieved  $\tau$ , estimated smoke TOA SWARF using smoke ADMs and ERBE ADMs, and TOA SWARF per optical thickness, and the number of samples for the statistics for the 6 surface IGBP types.  $\mu$  represents mean value and  $\sigma$  represents standard deviation. Flux unit:  $\text{Wm}^{-2}$ .

| Surface types | Mean $\alpha_{\text{TOA}}$ | # of sample | $\tau$ (0.64 $\mu\text{m}$ ) |          | Model SWARF |          | CERES SWARF |          | SWARF / $\tau$ |       |
|---------------|----------------------------|-------------|------------------------------|----------|-------------|----------|-------------|----------|----------------|-------|
|               |                            |             | $\mu$                        | $\sigma$ | $\mu$       | $\sigma$ | $\mu$       | $\sigma$ | Model          | CERES |
| Forest        | 0.145                      | 6211        | 1.51                         | 0.64     | -54.1       | 23.0     | -49.5       | 22.7     | -35.8          | -32.8 |
| *M Forest     | 0.159                      | 476         | 0.98                         | 0.56     | -35.5       | 23.3     | -41.1       | 19.8     | -36.2          | -41.9 |
| Savanna       | 0.144                      | 7234        | 1.36                         | 0.70     | -40.5       | 24.2     | -38.4       | 20.7     | -29.8          | -28.2 |
| Grassland     | 0.144                      | 3454        | 0.75                         | 0.46     | -32.5       | 28.7     | -34.3       | 26.0     | -43.3          | -45.7 |
| Wetland       | 0.149                      | 1125        | 0.90                         | 0.34     | -46.6       | 24.5     | -47.9       | 27.8     | -51.8          | -53.2 |
| Cropland      | 0.159                      | 365         | 0.62                         | 0.32     | -35.1       | 23.9     | -44.3       | 23.6     | -56.6          | -71.5 |

28

29

30

31

32

\*M Forest stands for mixed forest in the IGBP surface map.

Model SWARF means the TOA SWARF calculated using smoke ADMs

CERES SWARF means the TOA SWARF calculated using CERES ERBE-like data product.

33

34

35

36

37

1 **Figure legends**

2 Figure 1. Smoke single scattering albedo ( $\omega_0$ ) and asymmetry factor ( $g$ ) as function of  
3 wavelength used in this study

4 Figure 2. The calculated smoke ADMs with (a)  $\tau=0.36$ ,  $\omega_0=0.85$ ,  $\alpha_s=0.15$ ,  $\phi_0=36.9^\circ$ , (b)  
5  $\tau=1.10$ ,  $\omega_0=0.85$ ,  $\alpha_s=0.15$ ,  $\phi_0=36.9^\circ$ , (c)  $\tau=1.80$ ,  $\omega_0=0.85$ ,  $\alpha_s=0.15$ ,  $\phi_0=36.9^\circ$ , (d)  
6  $\tau=2.5$ ,  $\omega_0=0.85$ ,  $\alpha_s=0.15$ ,  $\phi_0=36.9^\circ$ , (e)  $\tau=0.36$ ,  $\omega_0=0.85$ ,  $\alpha_s=0.20$ ,  $\phi_0=36.9^\circ$ , (f)  
7  $\tau=1.8$ ,  $\omega_0=0.85$ ,  $\alpha_s=0.15$ ,  $\phi_0=36.9^\circ$ , (g)  $\tau=0.36$ ,  $\omega_0=0.85$ ,  $\alpha_s=0.20$ ,  $\phi_0=60^\circ$ , (h)  
8  $\tau=1.8$ ,  $\omega_0=0.85$ ,  $\alpha_s=0.15$ ,  $\phi_0=60^\circ$ , (i) the ERBE clear over land ADM and (j)  
9 ERBE partly cloudy over land.

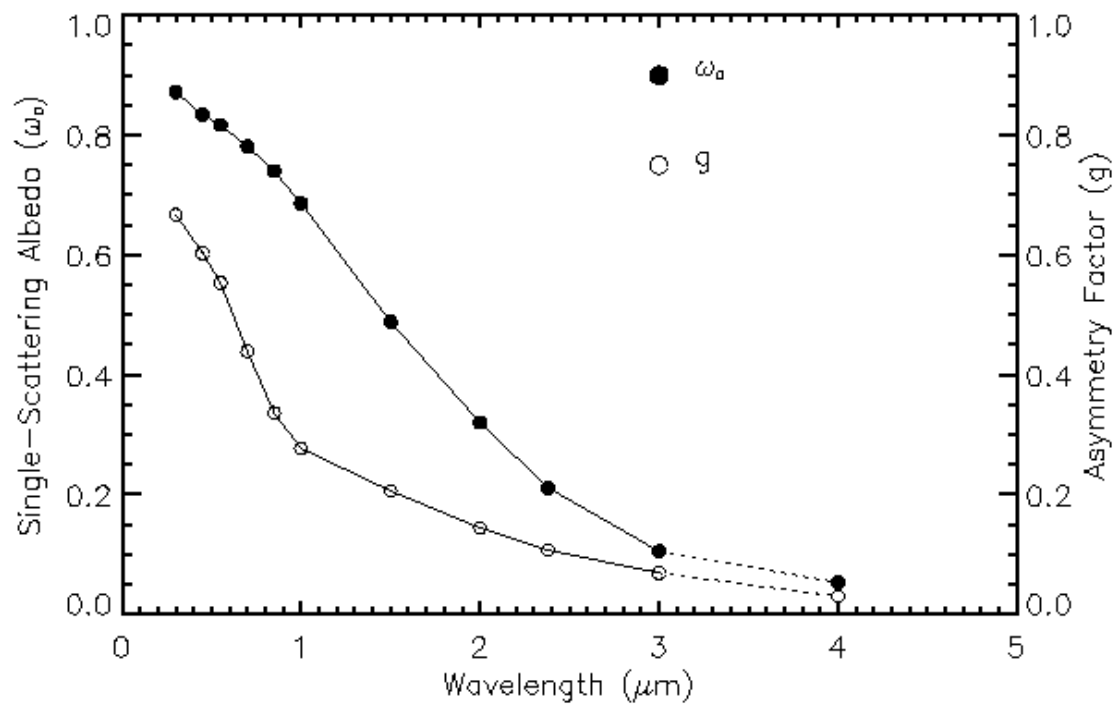
10 Figure 3. Sensitivity of smoke ADM as function of (a)  $\tau$ , (b)  $\omega_0$ , and (c) TOA clear-sky  
11 Albedo

12 Figure 4. (a) Sensitivity of smoke ADM as function of  $g$ , (b) influence of wavelength-  
13 dependent surface albedo on the smoke ADM values, and (c) the influence of  
14 surface BRDF on the smoke ADM values.

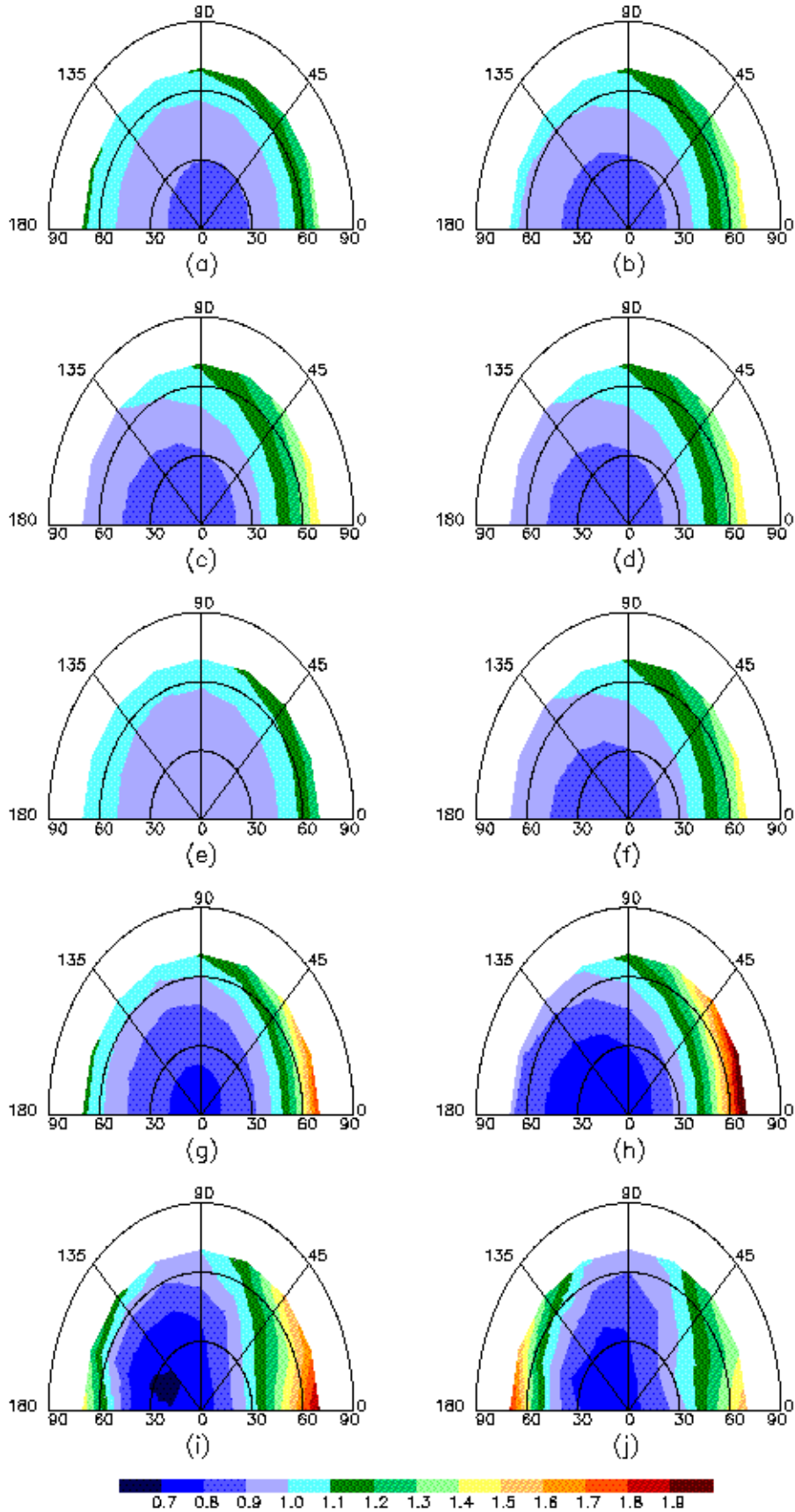
15 Figure 5. (a) VIRS channel 1 image for data file 9, (b) corresponding scene identification,  
16 black: clear, gray: cloud, white: smoke

17 Figure 6. Flow chart for smoke, cloud and clear-sky pixel identification from VIRS  
18 images over land in South America.

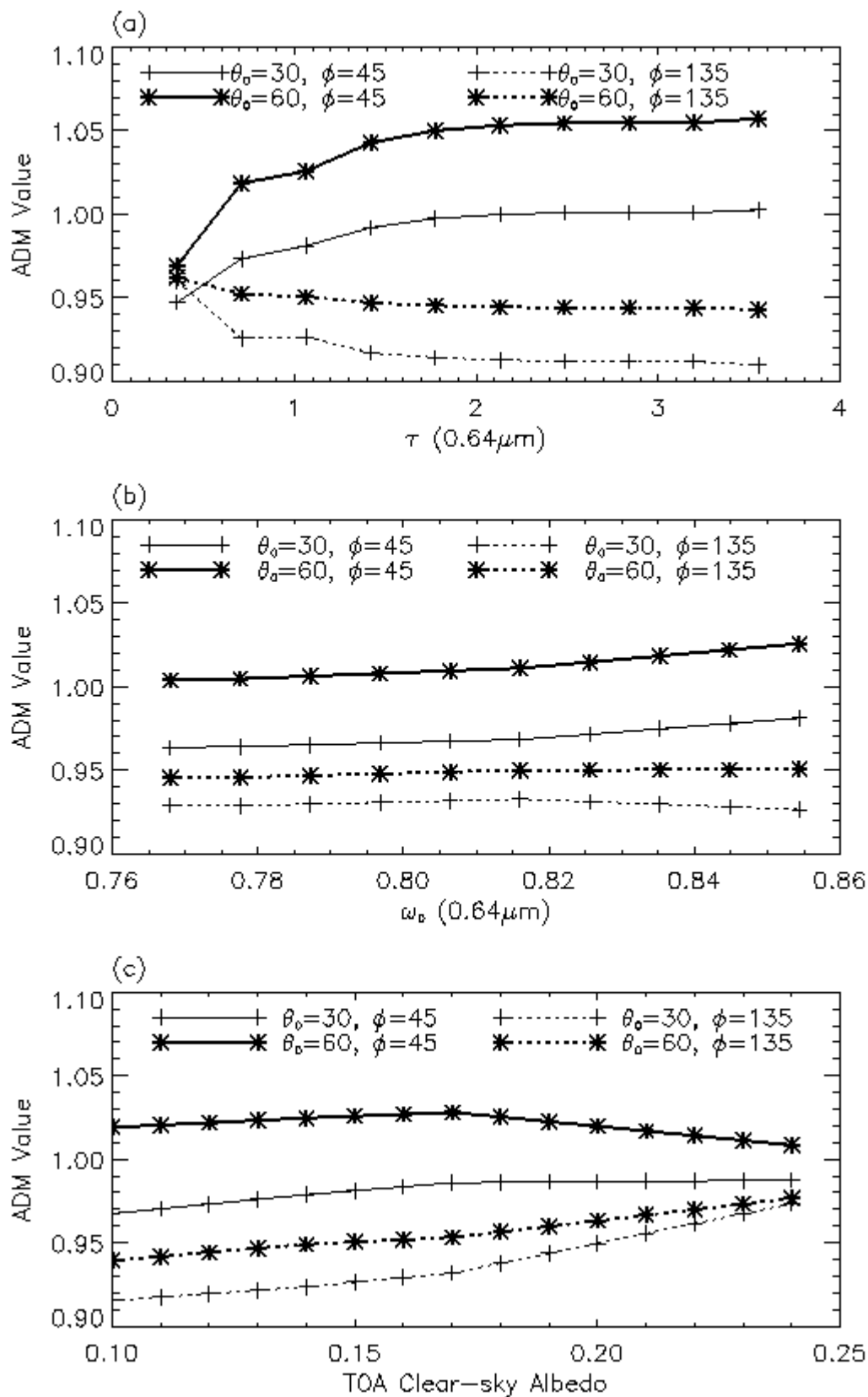
19 Figure 7. Scatter plot of TOA SW fluxes converted using smoke ADMs and CERES ES8  
20 ERBE-like SW fluxes.

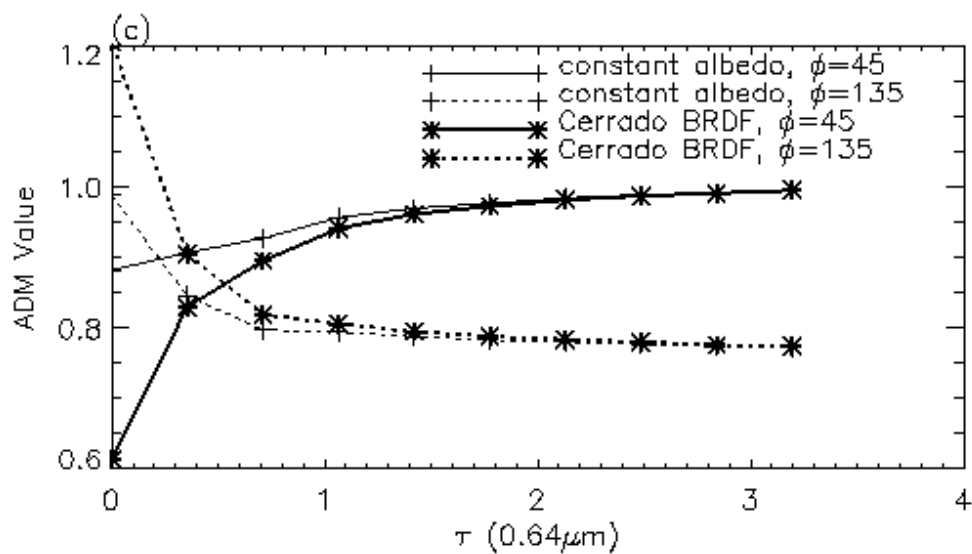
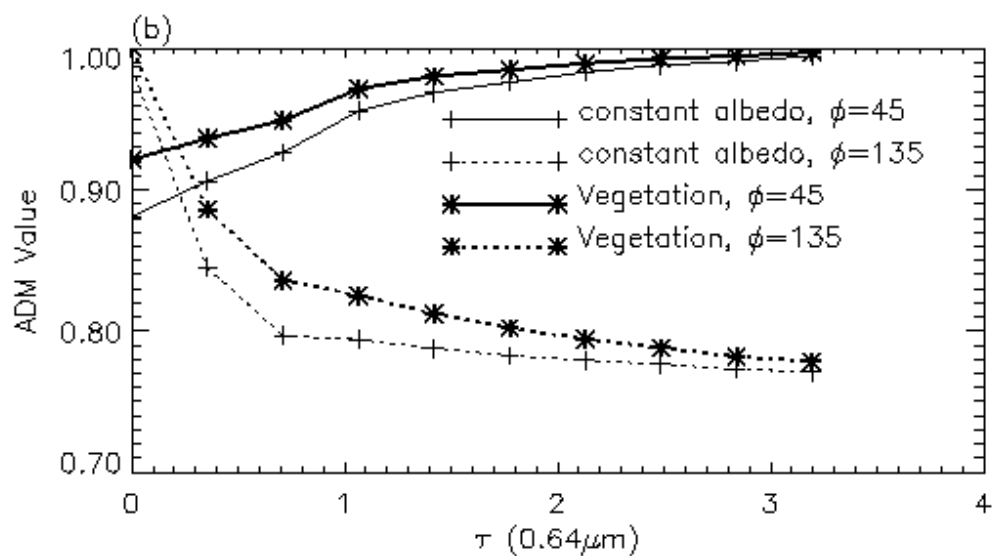
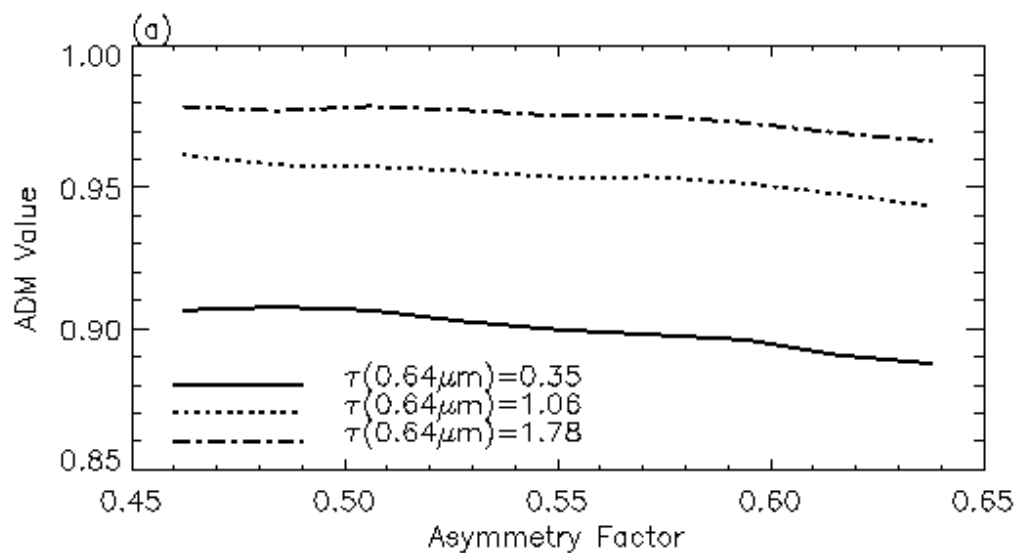


1

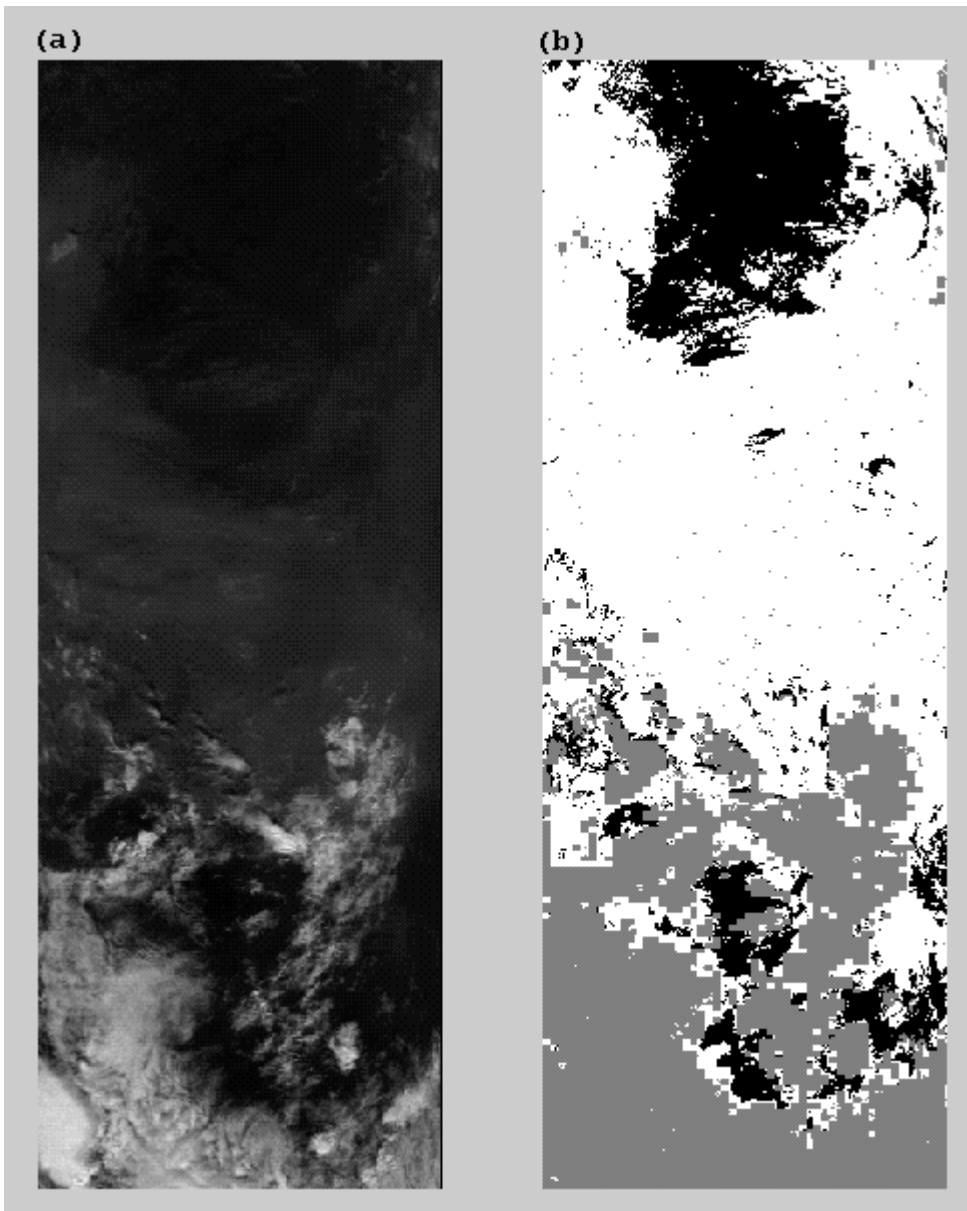




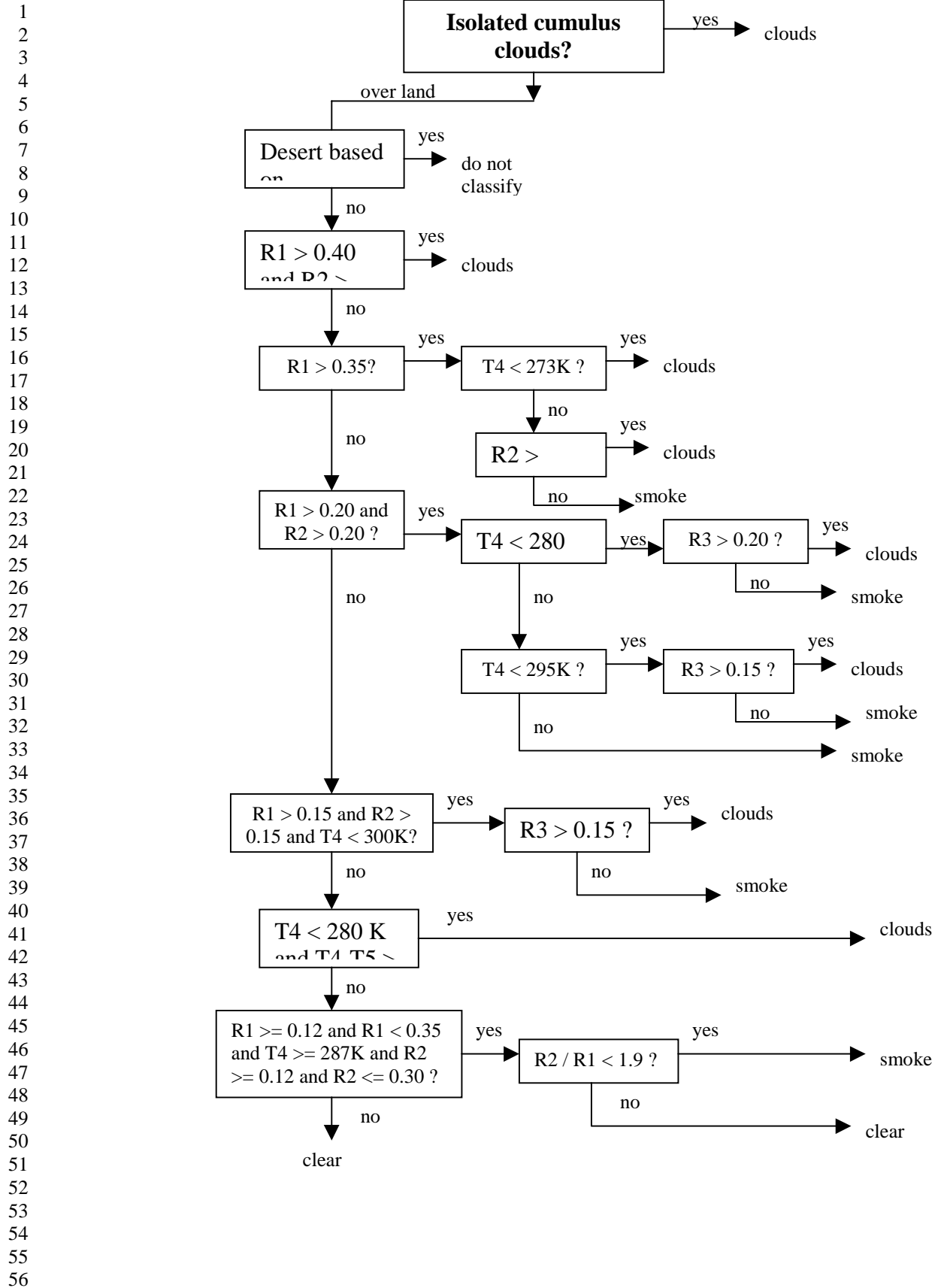


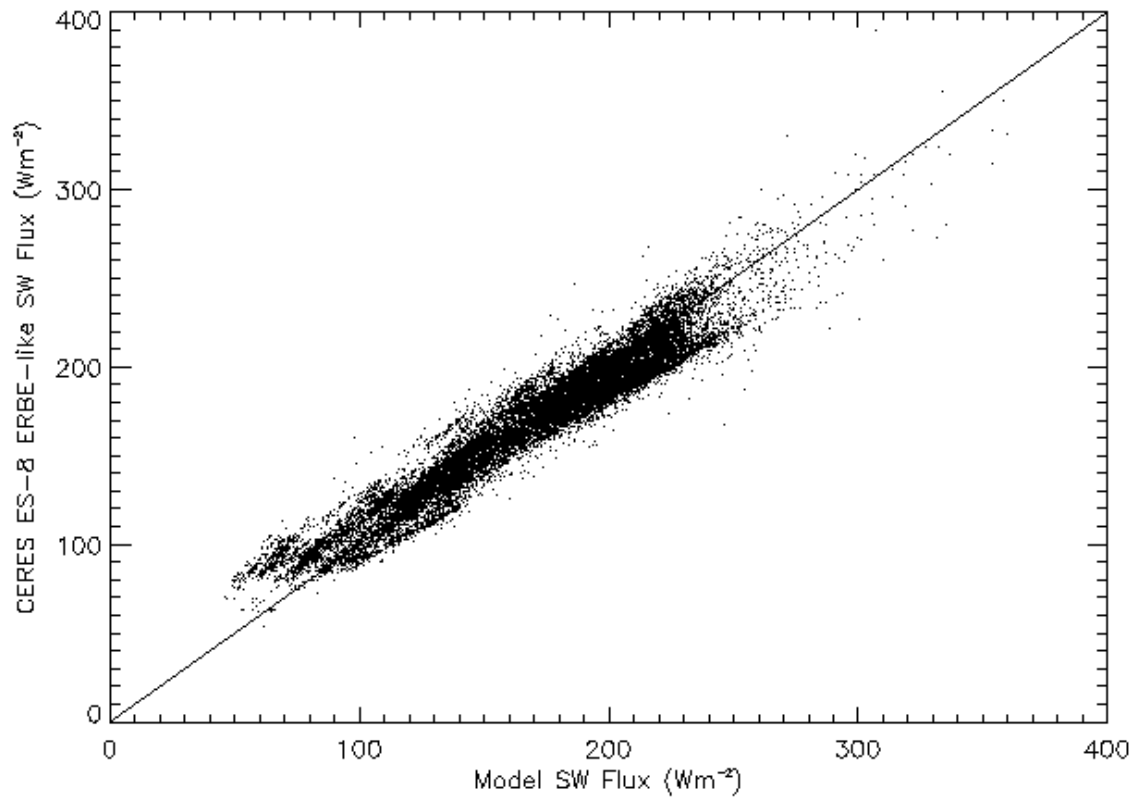






1





1